Research Square

Preprints are preliminary reports that have not undergone peer review.
They should not be considered conclusive, used to inform clinical practice,
or referenced by the media as validated information.

Low Earth orbit sits just below a self-sustaining debris cascade

Soung Sub LEE

spacein0320@gmail.com

Sejong University

Physical Sciences - Article

Keywords:

Posted Date: November 18th, 2026

DOI: https://doi.org/10.21203/rs.3.rs-11644514/v1

License: This work is licensed under a Creative Commons Attribution 4.0 International License.
Read Full License

Additional Declarations: There is **NO** Competing Interest.

Low Earth orbit sits just below a self-sustaining debris cascade

Soung Sub Lee[1,*]

[1]Department of Aerospace System Engineering, Sejong University, Seoul 05006, Republic of Korea

[*]Corresponding author. E-mail: spacein0320@sejong.ac.kr

Whether low Earth orbit (LEO) has already entered the runaway collisional cascade known as the Kessler syndrome[1,2] is central to the sustainable use of space. The answer hinges on the number of new lethal fragments that one fragment generates during its orbital lifetime, yet published assessments disagree on whether it exceeds unity[3–7]. Here we evaluate this LEO reproduction number, R_L, with an altitude-resolved next-generation operator for all 31,007 catalogued LEO objects, calibrating fragment residence from two decades of orbital decay of about 5,000 fragments. We find R_L = 0.67 (0.36–0.86) below 1,000 km. Large fragments live 3.5–6.5 times longer than the standard breakup model predicts, which reconciles simulations giving $R_L \approx 0.1$ with analytic assessments placing LEO above the threshold. LEO is subcritical, but a 50% increase in the collision cross-section of intact objects would make it critical. We also derive the closed-form minimum distance between orbits of a shell and a geometric scaling law for its capacity, and find that above about 430 km capacity is set by the debris cascade, not traffic geometry. R_L has been rising again since 2023, and 10,000 satellites above 800 km would take it above unity within a few years.

The rapid deployment of large constellations has turned the long-standing concern about collisional cascading[1,2] into an operational question. Environment reports find that the debris population of LEO would continue to grow even if launches stopped[8]. In 2025 Kessler and Lewis concluded that the intact population between about 520 and 1,000 km is at or above the runaway threshold[5], a conclusion subsequently used to assess the critical sizes of individual constellations[6]. Monte Carlo environment models built on the NASA standard breakup model (SBM)[9], in contrast, do not exhibit runaway growth on century time scales[10]. Because the policy implications of the two pictures are opposite, remediation

of an environment already past its tipping point, or management of one that still has a margin, it is important to determine which is correct and why they differ.

Growth of the debris population and runaway are not the same thing. Fragments are produced both by collisions between intact objects, which act as a source, and by collisions in which fragments themselves are the projectiles, which act as feedback. A population sustained mainly by the source grows towards a finite equilibrium; only when each fragment, during its lifetime, gives rise on average to more than one new fragment does the population grow without bound. Analytic particle-in-a-box models capture this distinction through the coefficients of a quadratic growth law[11]. The criterion is the basic reproduction number of epidemiology[12], and its use for debris has recently been proposed for a two-compartment model[7]. The quantity has not, however, been evaluated for the actual altitude-resolved population, nor has its key physical input, how long lethal fragments reside at a given altitude, been taken from observations. Nor has it been compared with the geometric limit on how many controlled satellites a shell can hold, for which no bound valid for every arrangement has been available. Here we supply these missing elements. New in this work are an altitude-resolved next-generation operator with two fragment types for the catalogued population; fragment residence calibrated from observed orbital decay; the closed-form minimum distance between orbits of a shell, an upper bound on its capacity that holds for every arrangement and the resulting geometric scaling law; and a reconstruction of R_L since 1980, which together show above which altitude the debris cascade, rather than geometry, limits capacity.

A reproduction number for orbital debris

In its simplest, single-region form, the reproduction number is

$$R_L = Y \frac{\tau}{\tau_c}, \tag{1}$$

the number Y of lethal fragments produced per collision times the ratio of the orbital lifetime τ of a fragment to the mean time between its collisions, $\tau_c = 1/(S\sigma v)$, where S and σ are the spatial density[1] and cross-section of the objects it can strike and v is the mean impact speed; equation (1) is the basic reproduction number[12] evaluated with the kinetic-theory collision rate[1,11]. For a shell of radius r containing N such objects, through which fragments descend at speed v_d, this becomes $R_L = Y$

$(N\sigma/4\pi r^2)(v/v_d)$: fragments per collision, times the fraction of the shell's area covered by targets, times the ratio of orbital to descent speed (Supplementary Information S7; this form follows directly from equation (1) and is convenient for hand calculation). We construct the next-generation operator G for fragments in LEO (Methods). A fragment born at altitude h descends under atmospheric drag through every altitude bin below h. While crossing a bin it collides with the objects there at a rate set by their cross-sections, number density and the mean impact speed, and each collision produces new fragments according to the SBM[9,13], which distinguishes catastrophic (≥40 J g^{-1}) from non-catastrophic impacts. New fragments are born with an altitude spread. We track two fragment types, catalogue-size fragments (≥10 cm), which active satellites can avoid, and lethal non-trackable fragments (1–10 cm), which they cannot. R_L is the spectral radius of G, which reduces to the single-region form when all altitudes are lumped together. The population enters through the residence-time distribution of catalogued objects over 10-km bins[14] (CelesTrak SATCAT, 23 October 2026; 35,394 objects in orbit), of which the 31,007 with perigees between 150 and 2,000 km are used, split into 16,363 active payloads, 3,247 intact derelicts and 11,397 catalogued fragments.

With the SBM mean mass-to-area ratio of about 10 kg m^{-2} for 10-cm-class fragments, the operator gives $R_L = 0.13$ for LEO below 1,000 km (Fig. 1). As an independent check we instrumented the open-source MIT Monte Carlo model MOCAT-MC[10], which uses its own propagator, JB2008 atmosphere and SBM implementation, to record for every simulated fragment cloud the expected number of fragments produced by its secondary collisions. Over 490 clouds in two 100-year no-launch runs, the measured generation ratio was 0.095–0.110, between the operator values for ≥10-cm fragments, the class MOCAT-MC follows (0.08), and for both fragment types (0.13). The two approaches therefore agree once they share the same fragment physics. The difference from analytic assessments must thus lies in that physics.

Fragment residence measured from orbital decay

R_L is proportional to the time a fragment spends at the altitudes where targets are dense, that is, inversely proportional to the product of its ballistic coefficient and the atmospheric density. Two-line-element drag terms (B^*) are often used to infer fragment mass-to-area ratios, but B^* is fitted against the

simplified density model internal to SGP4[15], which exceeds mean-solar-activity densities by factors of 14–17 at 800–865 km (Methods). Taken at face value, B^* implies median mass-to-area ratios of 70–190 kg m^{-2} for the three fragment clouds, values that, inserted in the operator, would place LEO well above the runaway threshold. After the density bias is removed, the same data give 5–11 kg m^{-2}, consistent with the SBM and with Space Fence measurements[16]. Because this correction uses a single density ratio and B^* also absorbs other unmodelled effects, these values only illustrate the size of the bias; residence is taken instead from orbital decay.

We therefore fitted the annual orbit histories (2007–2026) of 5,012 fragments of the Fengyun-1C anti-satellite test and the Cosmos 2251–Iridium 33 collision with an orbit-averaged King-Hele drag model[17] that uses the same density table as the operator (Methods). The fitted effective mass-to-area ratio is the quantity that sets residence in the operator; errors in the density table and the solar cycle are absorbed by construction at the calibration altitudes. Fragments with radar cross-sections below 0.1 m^2 have a median of 17 kg m^{-2} and a mean of 32 kg m^{-2}; the 78 large fragments (≥0.1 m^2, the class able to break up intact objects) have a median of 35 kg m^{-2} and a mean of 65 kg m^{-2}, with a long tail (Fig. 2). Large fragments thus reside about 3.5–6.5 times longer than the SBM mean implies, in line with earlier observations that collision clouds contain both lighter and heavier fragments than the model's central value[18]. A second, model-independent check, the fraction of each cloud that has re-entered, gives the same picture: after 18–20 years only 9% of the large Fengyun-1C fragments and 17% of the large Cosmos 2251 fragments have decayed.

Low Earth orbit is subcritical, but close

Because R_L depends on the mean residence time rather than the median, the physically appropriate input is the mean of the measured distribution. With it, the operator gives $R_L = 0.67$ for LEO below 1,000 km (Fig. 1). Because each fragment is followed by R_L fragments in the next generation, R_L^2 in the one after and so on, the cascade multiplies every fragment released by explosions or by collisions between intact objects by $1 + R_L + R_L^2 + \ldots = 1/(1 - R_L)$, a factor of about three at present. Using medians instead gives 0.36, and using the means of the longest-lived cloud (Fengyun-1C) gives 0.86. Of the full value, catastrophic collisions with ≥10 cm fragments contribute 0.43, non-catastrophic collisions add 0.08 and

lethal non-trackable fragments a further 0.16. The result is insensitive to the collision-avoidance success of active satellites (η = 0.99–0.999 changes R_L by less than 0.01, because derelicts dominate the targets) and moderately sensitive to the altitude spread of new fragments (0.60–0.81 for 50–150 km).

The operator also explains the disagreement in the literature. Inserting the fragment residence of the Kessler–Lewis assessment[5], a fragment mass-to-area ratio of 102 kg m^{-2}, with all other inputs unchanged, reproduces their conclusion, R_L = 1.33. SBM-based models[10] sit at the other end, $R_L \approx 0.1$, because they assign large fragments the residence of an average fragment. The observations lie between the two and, at the present population, below unity. The margin is modest: R_L reaches 1 when the collision cross-section presented by intact objects increases by a factor of 1.50 (1.17–2.83), equivalent to about 1,700 additional large derelicts of the current mix (a 53% increase in their number).

R_L increases steeply with altitude (Fig. 3a). The region below 800 km has R_L = 0.11 and that below 900 km 0.27; the 900–1,000 km band, where fragments live for centuries and rocket bodies are concentrated, accounts for most of the value below 1,000 km. The region evaluated here, below 1,000 km, hosts 92% of active satellites. Above it the environment has a different character. With almost no atmosphere, fragments persist for thousands of years, and R_L exceeds unity once the region is extended above about 1,200 km (an indicative value, because residence there is extrapolated beyond the calibrated altitudes), placing these shells on the supercritical side, as Kessler anticipated[2]. The cascade there is slow, unfolding over millennia, but it cannot be reversed by natural decay: any satellite abandoned above 1,000 km adds to it, which makes disposal at these altitudes a priority.

Where cascade physics, not geometry, sets capacity

The reproduction number limits how many satellites an altitude can host in a way that is distinct from the more familiar traffic limit[19], the number of controlled satellites that can be arranged so that none ever approach closer than a separation d. For satellites sharing a shell (common semi-major axis a and inclination i on circular orbits), the deferent–epicycle description of repeat-ground-track (RGT-Walker) constellations[20,21] gives the minimum distance between two orbits in closed form (equation (9) in Methods; see also ref. 22), and the phasings that lead to conflict form a thin band on the torus of node and argument-of-latitude differences (Fig. 4a). This band yields an upper bound on shell capacity, $N \lesssim$

$C(i)(a/d)^{4/3}$ to leading order in d/a, where $C(i) = (16\pi^2/3)(\sin^2 i\,|\cos i|/3)^{1/3}$ depends only on the inclination (C = 18.5 for a sun-synchronous shell), and exact searches over Walker lattices[23] find about 5.6 (a/d) ln(a/d) satellites for $10 \le a/d \le 500$ (Fig. 4b), a factor of order ln(a/d) more than non-self-intersecting constellations[22] and comparable to closely packed shells constructed explicitly[24]; unlike those constructions, the bound applies to every arrangement. Shells of equal inclination can be stacked radially at the navigation precision, and Starlink shells already hold their radial positions to within 80 m (95%; Supplementary Information S6). The derivations, the lattice data and the analysis of resonant phasing between shells are given in Supplementary Information S1–S6; the closed-form distance, the bound and the scaling law are new results of this work.

Comparing the two limits per 50-km shell (Fig. 3b) shows that geometry is not the binding constraint in most of LEO. For a failure rate of 1% per year and the measured fragment residence, the critical number of satellites that keeps R_L below unity falls from 1.8×10^5 at 475 km to 2.1×10^3 at 775 km, 3.4×10^2 at 875 km and about 60 at 975 km, a factor of about ten every 140 km, reflecting the steep increase of residence time with altitude. Even with the conservative separations needed to ride out a geomagnetic storm on ground-based orbit determination (in-shell separation d_s = 42 km, radial separation d_r = 0.67 km; assumed scenario values, Methods), the geometric ceiling is about 3.5×10^5 per 50-km shell; the two limits cross near 430 km. Because a larger separation lowers the geometric ceiling, this crossing moves to higher altitude only if the required separations exceed these values; smaller separations move it lower. Below about 430 km, the number of satellites a shell can host is limited by traffic geometry; above it, by the debris cascade. The present Starlink shells at 465–485 km (about 8,800 satellites) use about 5% of the cascade limit of their shell, whereas a single 1,000-satellite constellation with the same reliability at 875 km would by itself exceed it. The same 4,000 satellites that would raise R_L from 0.67 to 1.6 in a shell at 775 km leave it unchanged, to within 10^{-4}, at 575 km: because fragments only descend, R_L is set by the most critical altitude band, and additions lower down do not change it until their own shell approaches its limit.

Past and future of the reproduction number

Because the catalogue records launch and decay dates, R_L can be reconstructed backwards in time (Methods). It rose from 0.19 in 1980 to 0.58 in 2000, as rocket bodies and payloads accumulated at 700–1,000 km, and then levelled off at 0.62–0.64 between 2005 and 2023, the period in which debris-mitigation guidelines took effect (Fig. 5a). The Fengyun-1C and Iridium–Cosmos breakups barely changed it, because R_L is set by the massive targets that fragments strike, not by the fragments a breakup adds. Since 2023 R_L has risen again, at 0.007 per year, 2.5 times the 2000–2022 rate; over the same period the number of rocket bodies left in orbits with mean altitude 700–1,000 km increased from 3.4 to 12.8 per year.

Projecting these trends forward (Fig. 5b), the 2023–2026 rate brings R_L to unity around 2072 for the mean residence (2046 for the longest-lived cloud; after 2100 for the median), whereas the 2000–2022 rate keeps it below unity this century except for the longest-lived cloud (2065). Removing the ten most massive derelicts per year from 700–1,000 km from 2030 keeps R_L below unity to 2100 even at the recent rate. Large additions change the picture within years. Ten thousand satellites at 800–1,000 km, deployed over 2027–2035 with a failure rate of 1% per year, take R_L above unity in 2028, when about 10^3 of them are in orbit; 7×10^5 satellites, an illustrative figure for the largest proposed constellations combined, spread over 340–600 km do so by 2029, whereas the same number confined below 450 km brings R_L just above unity (1.04 in 2050) rather than far beyond it. These are scenarios rather than forecasts, but they show that the date at which LEO becomes supercritical is set mainly by what is placed, and left, above about 450 km.

Discussion

Over most of low Earth orbit, capacity is limited by debris, not by geometry. Our results reconcile two conflicting views of the stability of LEO. The environment is not yet in a self-sustaining cascade, but it is closer to one than breakup-model-based simulations suggest, and the margin is consumed by the accumulation of large derelicts, including satellites that fail or are abandoned, rather than by operating satellites as such. A constellation of 10^5 satellites with a 1% annual failure rate leaves about 10^3 uncontrolled spacecraft per year; if these remained above 700 km for decades, they would erase the

remaining margin within a few years. Because the critical load falls by more than three orders of magnitude between 475 and 975 km, the choice of operating altitude is the strongest lever available to operators, while removal of large derelicts from the 700–1,000 km band is the most effective remediation. The reconstruction shows that this margin, stable for two decades, is again being consumed, now by upper stages left in high LEO.

Three limitations should be noted. First, masses of catalogued intact objects are inferred from radar cross-sections with assumed area densities (Methods); a factor-of-two error in cross-section changes R_L proportionally, and the same error in mass changes it by less, through the $M^{0.75}$ dependence of the yield. Second, the breakup model is used for fragment counts, whereas residence is taken from observations; the agreement of fragment counts with catalogued debris clouds has been established elsewhere[9,16]. Third, R_L is a linear threshold; it does not describe the time to reach equilibrium, and stochastic fluctuations near criticality can trigger cascades earlier than mean-field estimates suggest[7]. Because residence time enters linearly and is now measured, the largest remaining uncertainty is the lethality and fragment yield of collisions between fragments and large intact objects, which can be constrained by future breakup observations.

Methods

Catalogue and population

We used the CelesTrak satellite catalogue[14] of 23 October 2026 and retained Earth-orbiting objects without a decay date and with perigee between 150 and 2,000 km. Objects were classified as active (payloads with operational status +, P, B, S or X), intact derelicts (other payloads, rocket bodies and unknown objects) and fragments (catalogue type DEB). Missing radar cross-sections (RCS) were filled with the class median. The collision cross-section was taken as max(RCS, 0.05 m^2); intact masses were estimated as 400 kg m^{-2} × RCS (an assumed area density typical of payloads and rocket bodies; clipped to 50–9,000 kg) and fragment masses as 30 kg m^{-2} × RCS (0.3–200 kg; consistent with the measured fragment mass-to-area ratios, Fig. 2). Because objects on eccentric orbits cross several altitude bins, the time fraction that each object spends in 10-km altitude bins between 200 and 2,000 km follows from Kepler's equation for its elliptical orbit between perigee and apogee[1]; near-circular objects (apogee minus perigee < 5 km) are assigned to a single bin.

Breakup yields and lethality

Fragment numbers follow the NASA SBM[9,13],

$$N(\geq L_c) = 0.1\, M^{0.75}\, L_c^{-1.71}, \tag{2}$$

with M the sum of the masses for catastrophic collisions (specific energy ≥40 J g^{-1}) and $M = m_p v^2$ (v in km s^{-1}) for non-catastrophic ones, where m_p is the projectile mass (kg) and L_c the characteristic length (m) of the fragments; non-catastrophic yields of ≥10 cm fragments are capped by the ejected mass. Projectile sizes are integrated over the SBM size distribution ($L^{-2.71}$) separately for 1–10 cm and 10–100 cm, with the SBM size–mass relation[9,13]. The mean impact speed is 10 km s^{-1}. Because both the collision rate and, through the impact energy, the catastrophic threshold and the non-catastrophic yields depend on this speed, taking 9 or 11 km s^{-1} instead gives R_L = 0.52 or 0.85; the conclusion that LEO below 1,000 km is subcritical is unchanged. Active satellites avoid ≥10 cm fragments with success η = 0.999 and cannot avoid 1–10 cm fragments.

Next-generation operator

For projectile type t and produced type t', the yield-weighted target cross-section in bin h is

$$A_{tt'}(h) = \sum_j W_j(h)\, f_t(j)\, \sigma_j\, Y_{tt'}(M_j), \tag{3}$$

where W_j is the residence fraction of object j, σ_j its collision cross-section, M_j its mass (both derived from radar cross-sections; see Catalogue and population), f_t the avoidance factor ($f_t(j) = 1 - \eta = 0.001$ for ≥10-cm projectiles striking active satellites, which manoeuvre with an assumed success $\eta = 0.999$, and $f_t(j) = 1$ otherwise, including all 1–10-cm projectiles) and Y the expected yield from equation (2). By the kinetic (particle-in-a-box) theory[1,11], a fragment in bin h'' of width Δz collides at the rate $vA/(4\pi r^2 \Delta z)$ and remains there for the time $\Delta z/\dot{z}_t$, given by the circular-orbit drag decay rate[17]. A fragment of type t crossing bin h'' produces on average

$$w_{tt'}(h'') = \frac{v\, A_{tt'}(h'')}{4\pi r^2\, \dot{z}_t(h'')}, \qquad \dot{z}_t = \rho(h'')\, B_t \sqrt{\mu r} \tag{4}$$

new fragments, where $\dot{z}_t$ is the drag-induced descent rate of a type-t fragment, r the orbital radius of bin h'', ρ the atmospheric density, μ Earth's gravitational parameter, C_D the drag coefficient, A/m the area-to-mass ratio and $B_t = C_D A/m$. A fragment born at h visits all bins $h'' \le h$; new fragments are born with a Gaussian altitude spread of 75 km (50–150 km in sensitivity tests). With U the upper-triangular descent matrix ($U_{h''h} = 1$ if $h'' \le h$ and 0 otherwise) and K the birth kernel (the Gaussian altitude distribution of new fragments), $\circ$ denoting the element-wise product, the operator and its reproduction number are

$$G_{t't} = (U \circ w_{tt'})K, \qquad R_L = \varrho(G), \tag{5}$$

where ϱ denotes the spectral radius of G restricted to the region below a chosen altitude (1,000 km unless stated), following the next-generation formalism[12]; because G is non-negative, the ratio of successive fragment generations converges to $\varrho(G)$ for any initial fragment distribution (Perron–Frobenius theorem), so R_L is the asymptotic factor by which each generation multiplies the next. The ingredients of equations (2)–(5), breakup yields, kinetic collision rates and drag decay, are standard[1,9,17]; their combination into an altitude-resolved operator with two fragment types, and the calibration of its residence from observed decay, are new in this work. A mean-solar-activity density table based on NRLMSISE-00[25] is used throughout; for the calibrated case, its errors are absorbed by the residence fit

described below. R_L converges as the altitude bins are refined: bins of 5, 10, 20 and 50 km give R_L = 0.676, 0.672, 0.657 and 0.614, so R_L increases monotonically as the bins are refined and the 10-km value lies within 1% of the 5-km value. The operator result is cross-checked against an independent Monte Carlo model.

Fragment residence from orbital decay

From Space-Track two-line-element histories we extracted, for each catalogued fragment of Fengyun-1C, Cosmos 2251 and Iridium 33, one element set per year (mean motion and eccentricity). For the 5,012 fragments with at least three annual records spanning at least three years and initial perigee above 300 km, we integrated the King-Hele orbit-averaged decay equations[17]

$$\frac{da}{dt} = -B\rho_p\sqrt{\mu a}\, e^{-c}[I_0(c) + 2e\, I_1(c)], \qquad \frac{de}{dt} = -B\rho_p\sqrt{\frac{\mu}{a}}\, e^{-c}\left[I_1(c) + \frac{e}{2}\big(I_0(c) + I_2(c)\big)\right] \quad (6)$$

with ρ_p the density at perigee, $c = ae/H$, H the local density scale height and I_n modified Bessel functions of order n, a and e the semi-major axis and eccentricity, μ Earth's gravitational parameter and $B = C_D A/m$ the ballistic coefficient (5-day steps, density table and scale heights as in the operator), for 40 ballistic coefficients between 10^{-3} and 3 m^2 kg^{-1}, and interpolated the coefficient that reproduces the observed decrease in semi-major axis. The effective mass-to-area ratio is $2.2/B$. Objects whose semi-major axis decreased by less than 50 m were excluded. Because the same density table is used in the fit and in equation (4), the product $B\rho$, which alone determines residence, is reproduced irrespective of density-table errors at the calibration altitudes (790–865 km). For comparison, B^*-based estimates were corrected by the ratio of the SGP4 internal density[15],

$$\rho_{\mathrm{SGP4}}(h) = 2.461 \times 10^{-8}\left(\frac{120-78}{h-78}\right)^4 \ \mathrm{kg\ m^{-3}}, \quad (7)$$

to the mean-solar density (a factor of 14 at 800 km and 17 at 865 km; h is the altitude in km).

Independent verification with MOCAT-MC

The MOCAT-MC code[10] (MIT licence) was run without modification of its physics under GNU Octave, with compatibility functions for date handling and three statistics functions. We tagged every fragment produced by a simulated collision with a cloud identifier and, at every 5-day step, accumulated for each

cloud the collision probability of candidate pairs (MOCAT cube method) multiplied by the SBM yield of that pair. The generation ratio of a cloud is the accumulated expected yield divided by its number of fragments. Two 100-year no-launch runs from the 2023 initial population, with collision sampling increased threefold to obtain 490 clouds, gave 0.095–0.110 for clouds below 1,000 km and 0.14–0.17 for 800–1,000 km, stable for tracking horizons of 50–90 years. MOCAT-MC follows fragments ≥10 cm only; for these, the operator with SBM fragment properties gives $R_L = 0.08$, and including 1–10-cm fragments gives 0.13 (Fig. 1), so the two values bracket the simulated ratio. The simulation also starts from the 2023 population and declines without launches, whereas the operator uses the October 2026 catalogue. Increased sampling raises the debris background and therefore biases this check upwards.

Critical loading of a shell

The margin λ^* is the factor by which the cross-sections σ_j of all intact objects in equation (3) must be multiplied for $\varrho(G)$ to reach unity; because intact objects dominate the targets, $\lambda^* \approx 1/R_L$, and the full calculation gives 1.50. To obtain $N^*(h)$, we added N new satellites (800 kg, 10 m^2) uniformly to a 50-km shell centred at h, with annual failure rate $\lambda_f = 1\%$ and avoidance success $\eta = 0.999$. Failed satellites descend with $C_D A/m = 0.07$ m^2 kg^{-1}; by flux conservation (the steady-state continuity equation of debris-cloud models[26]) their steady-state number in the bin at altitude h is

$$D_{\mathrm{new}}(h) = \frac{\Delta z}{\dot{z}_D(h)} \sum_{h' \geq h} \lambda_f \; n(h'), \tag{8}$$

where $n(h')$ is the number of new satellites in bin h', $\dot{z}_D$ the descent rate of failed satellites and Δz the bin width. N^* is the largest N for which the full-model R_L of equation (5) remains below unity, found by bisection on top of the present catalogue.

Single-shell geometry

For two circular orbits of radius a and inclination i whose nodes and arguments of latitude differ by $\Delta\Omega$ and Δu, the minimum distance over time is (derived in this work from the deferent–epicycle form of the RGT-Walker solution[20,21]; Supplementary Information S1)

$$\frac{d_{\min}}{a} = 2\left|\cos^2\frac{i}{2}\sin\frac{\Delta\Omega+\Delta u}{2} - \sin^2\frac{i}{2}\sin\frac{\Delta\Omega-\Delta u}{2}\right|. \tag{9}$$

Its repeat-ground-track Walker (RGT-Walker) form, the conflict band and the upper bound on shell capacity, the exhaustive search over cyclic Walker lattices (all F for each $T \leq 6.5(a/d)^{4/3}$, each found lattice being a certified configuration), the resonance lemma, and the radial-stacking analysis including the separations assumed in Fig. 3b are given in Supplementary Information S2–S6. The in-shell separations are three times the relative along-track prediction error of two satellites, $d_s = 3\sqrt{2}\,\sigma_{at}$, where σ_{at} is the 24-hour along-track error of one satellite: about 0.28 km for ground-based orbit determination in quiet conditions and 10 km during geomagnetic storms, a conservative value above the several-kilometre errors reported within one day during the May 2024 storm[27]. This gives d_s = 1.2 km and 42 km. The quiet-time radial separation, d_r = 0.08 km, follows from the Starlink data of Supplementary Information S6; the storm-time value, 0.67 km, is assumed ($d_r = 3\sqrt{2}\,\sigma_r$, with an assumed radial error of one satellite σ_r = 0.16 km). Because the geometric ceiling scales as $1/d_r$, doubling d_r halves it and raises its crossing with the cascade limit from about 430 km to about 475 km; the conclusion that cascade physics sets capacity over most of LEO is unchanged. The crossing altitude $h_\times$ is where the computed $N^*(h)$ equals the geometric ceiling $N_{geo} = (\Delta h/d_r) \times 5.6\,(a/d_s)\ln(a/d_s)$, which varies by less than 1% between 400 and 500 km; because $N^*(h)$ falls by about a factor of ten every 140 km, $h_\times \approx 475$ km − 140 km × $\log_{10}(3.5\times10^5/1.8\times10^5) \approx 430$ km.

Historical reconstruction and scenarios

For each year from 1980 to 2026 we selected the catalogued objects launched before and decayed after 1 January of that year. Objects that have since decayed, and uncontrolled objects still in orbit, were placed at the altitude from which drag brings them to their catalogued state in the elapsed time, using the circular-orbit lifetime[17]

$$L(h) = \int_{150\ \mathrm{km}}^{h} \frac{dz}{\dot{z}(z)}, \qquad h(t) = L^{-1}[L(h_{\mathrm{cat}}) + t_{\mathrm{cat}} - t], \tag{10}$$

where h_{cat} is the catalogued altitude at the catalogue epoch t_{cat}, z the altitude and $\dot{z}$ the circular-orbit descent rate of equation (4), with the density table of the operator, C_DA/m = 0.0055 m^2 kg^{-1} for intact objects and 0.069 m^2 kg^{-1} for debris, and $t_{cat} - t$ replaced by the time to decay for decayed objects; active payloads keep their catalogued altitude, and a payload counts as active if it is active now or was launched within the preceding 7 years. The reconstruction reproduces R_L = 0.671 for the present

catalogue. For the projections, the target cross-section of equation (3) was extended linearly in time at the rate observed in 2000–2022 or in 2023–2026. Added satellites (800 kg, 10 m^2) were deployed linearly over 2027–2035 and maintained thereafter; failed satellites become derelicts (C_DA/m = 0.07 m^2 kg^{-1}) whose number per bin, $D(h, t)$, obeys

$$\frac{\partial D}{\partial t} = \lambda_f \, n(h,t) - \frac{\partial}{\partial h}[\dot{z}_D(h)\, D], \tag{11}$$

the time-dependent form of equation (8) (the continuity equation[26]), integrated with an implicit upwind scheme. Active removal subtracts the contributions of the most massive derelicts with mean altitude 700–1,000 km, ten per year from 2030 (400 objects in total). $R_L(t)$ is evaluated with equations (3)–(5) at every year.

Limitations

The density table represents mean solar activity; outside the calibration altitudes (790–865 km), the residence time scales with its local shape, so that values above 1,000 km, where the density table is extrapolated and above about 1,100 km fragment lifetimes exceed 10^3 years, are indicative only. Masses from radar cross-sections are uncertain by about a factor of two. Radar cross-sections are not published for objects launched since 2023, which were assigned the class median; because recent upper stages are heavier than the median intact object, the recent rise of R_L is probably underestimated. The reconstruction neglects past manoeuvres of objects that are now inactive. The linear operator neglects depletion of targets and the explicit time dependence of the solar cycle, and is intended as a threshold rather than a forecast. A complementary, shell-wise stability analysis of linearized source–sink models is given in ref. 28.

Use of AI tools

The author conceived the study, formulated the model, selected the data, and checked every derivation and result. A large language model (Claude, Anthropic) assisted with code development, numerical exploration and drafting of the text. All reported numbers and figures are generated by the author's MATLAB code (see Code availability); the operator results (R_L = 0.13, 0.36, 0.67 and 1.33 and the margin of 1.50) were reproduced with the same code under GNU Octave, and the operator was cross-

checked against the independent MOCAT-MC Monte Carlo model (Methods). No figure or image was generated by the language model. The author takes full responsibility for the content.

Data availability

The satellite catalogue is publicly available from CelesTrak (https://celestrak.org/satcat). Two-line-element histories are available from Space-Track.org after registration. The Starlink element sets used are available at https://github.com/j0028036/tle_data. Derived data supporting the findings of this study are available from the corresponding author upon reasonable request.

Code availability

The MATLAB code used in this study is available from the corresponding author upon reasonable request. MOCAT-MC is available at https://github.com/ARCLab-MIT/MOCAT-MC.

References

1. Kessler, D. J. & Cour-Palais, B. G. Collision frequency of artificial satellites: the creation of a debris belt. *J. Geophys. Res.* **83**, 2637–2646 (1978).

2. Kessler, D. J. Collisional cascading: the limits of population growth in low Earth orbit. *Adv. Space Res.* **11**, 63–66 (1991).

3. Liou, J.-C. & Johnson, N. L. Risks in space from orbiting debris. *Science* **311**, 340–341 (2006).

4. Liou, J.-C. & Johnson, N. L. Instability of the present LEO satellite populations. *Adv. Space Res.* **41**, 1046–1053 (2008).

5. Kessler, D. J. & Lewis, H. G. Critical number of spacecraft in low Earth orbit: a new assessment of the stability of the orbital debris environment. In *Proc. 9th European Conference on Space Debris* (ESA Space Debris Office, 2025).

6. Lewis, H. G. Critical sizes of satellite constellations. Preprint at https://arxiv.org/abs/2607.29644 (2026).

7. Behera, P., Gopalan, A. S. & Honnappa, H. Stochastic dynamics of low Earth orbit near full capacity. Preprint at https://arxiv.org/abs/2608.23491 (2026).

8. ESA Space Debris Office. *ESA's Annual Space Environment Report* (European Space Agency, 2025).

9. Johnson, N. L., Krisko, P. H., Liou, J.-C. & Anz-Meador, P. D. NASA's new breakup model of EVOLVE 4.0. *Adv. Space Res.* **28**, 1377–1384 (2001).

10. Jang, D. et al. A new Monte-Carlo model for the space environment. Preprint at https://arxiv.org/abs/2405.10430 (2024).

11. Talent, D. L. Analytic model for orbital debris environmental management. *J. Spacecr. Rockets* **29**, 508–513 (1992).

12. Diekmann, O., Heesterbeek, J. A. P. & Metz, J. A. J. On the definition and the computation of the basic reproduction ratio R_0 in models for infectious diseases in heterogeneous populations. *J. Math. Biol.* **28**, 365–382 (1990).

13. Krisko, P. H. Proper implementation of the 1998 NASA breakup model. *Orbital Debris Q. News* **15**(4), 1–10 (2011).

14. Kelso, T. S. SATCAT: satellite catalog. CelesTrak https://celestrak.org/satcat (accessed 23 October 2026).
15. Hoots, F. R. & Roehrich, R. L. *Models for Propagation of NORAD Element Sets*. Spacetrack Report No. 3 (US Air Force Aerospace Defense Command, 1980).
16. Smith, T., Folcik, Z. & Linares, R. Challenges in orbital debris modeling: a comparative analysis of NASA SBM and Space Fence data. In *Proc. Advanced Maui Optical and Space Surveillance Technologies Conference* (AMOS, 2024).
17. King-Hele, D. *Satellite Orbits in an Atmosphere: Theory and Applications* (Blackie, 1987).
18. Stansbery, E. G. & Matney, M. J. A comparison of catastrophic on-orbit collisions. In *Proc. Advanced Maui Optical and Space Surveillance Technologies Conference* (AMOS, 2008).
19. Lavezzi, G., Lifson, M., Servadio, S. & Linares, R. Orbital tolerance and intrinsic orbital capacity for electric propulsion constellations. *J. Spacecr. Rockets* https://doi.org/10.2514/1.A35875 (2024).
20. Lee, S. S. Closed-form solution of repeat ground track orbit design and constellation deployment strategy. *Acta Astronaut.* **180**, 588–595 (2021).
21. Lee, S. S. Explicit mathematical formulation and coverage consistency of satellite constellation designs for repeating ground track orbits. *IEEE Trans. Aerosp. Electron. Syst.* **60**, 1102–1112 (2024).
22. Arnas, D. & Linares, R. Non-self-intersecting trajectories and their applications to satellite constellation design and orbital capacity. *J. Guid. Control Dyn.* https://doi.org/10.2514/1.G007208 (2022).
23. Walker, J. G. Satellite constellations. *J. Br. Interplanet. Soc.* **37**, 559–572 (1984).
24. Lifson, M., Arnas, D., Avendaño, M. & Linares, R. A method for generating closely packed orbital shells and the implication on orbital capacity. In *AIAA SciTech Forum* https://doi.org/10.2514/6.2023-2170 (2023).
25. Picone, J. M., Hedin, A. E., Drob, D. P. & Aikin, A. C. NRLMSISE-00 empirical model of the atmosphere: statistical comparisons and scientific issues. *J. Geophys. Res.* **107**, 1468 (2002).
26. Letizia, F., Colombo, C. & Lewis, H. G. Multidimensional extension of the continuity equation method for debris clouds evolution. *Adv. Space Res.* **57**, 1624–1640 (2016).

27. Parker, W. E. & Linares, R. Satellite drag analysis during the May 2024 Gannon geomagnetic storm. *J. Spacecr. Rockets* https://doi.org/10.2514/1.A36164.

28. Turyshev, S. G. Orbital debris in Earth orbit: operations, stability, control, and market formation. *Acta Astronaut.* **247**, 652–668 (2026).

Acknowledgements

This work was supported by Institute of Information & communications Technology Planning & Evaluation (IITP) under the metaverse support program to nurture the best talents (IITP-2026-RS-2023-00254529) & the development of metaverse-based space object orbital information visualization and linkage technology (No. 1711195701) grant funded by the Korea government(MSIT)

Author contributions

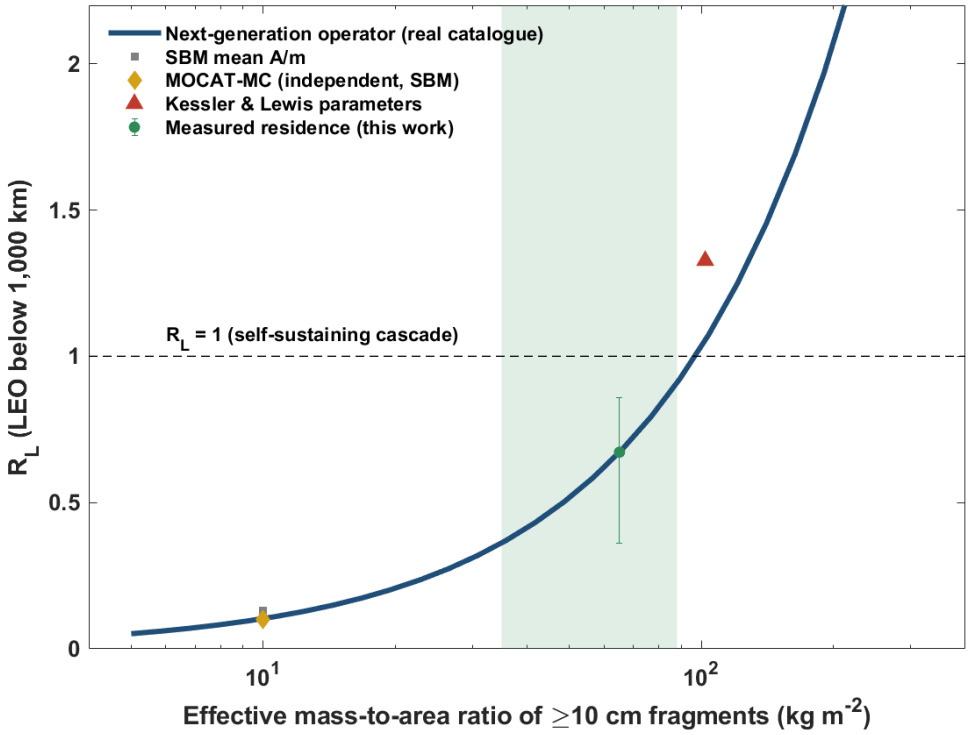
S.S.L. conceived the study, performed the analyses and wrote the manuscript.

Competing interests

The author declares no competing interests.

Additional information

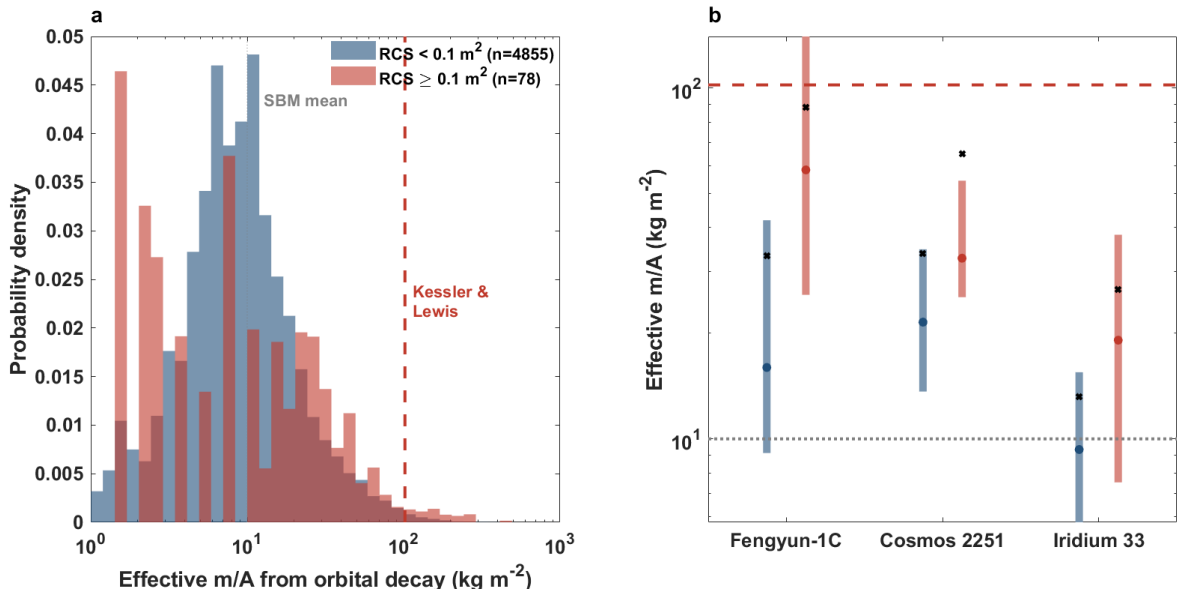
Correspondence and requests for materials should be addressed to Soung Sub Lee (spacein0320@sejong.ac.kr).



441

442 **Fig. 1 | Reproduction number of debris fragments in LEO.** R_L of the next-generation operator for
443 the October 2026 catalogue below 1,000 km as a function of the effective mass-to-area ratio of ≥10 cm
444 fragments (1–10 cm fragments scaled in proportion). Grey square: standard breakup model (SBM) mean
445 mass-to-area ratio. Yellow diamond: generation ratio measured independently in the MOCAT-MC
446 Monte Carlo model, which uses SBM fragment properties and follows fragments ≥10 cm only. Red
447 triangle: fragment residence of the Kessler–Lewis assessment (102 kg m^{-2}). The SBM and Kessler–
448 Lewis cases apply one mass-to-area ratio to both size classes and therefore lie slightly above the curve.
449 Green circle and band: residence measured from the orbital decay of about 5,000 fragments; the circle
450 uses the mean (R_L = 0.67), the error bar spans the median-based value (0.36) and the longest-lived cloud
451 (0.86), and the shaded band the corresponding mass-to-area range. The dashed line marks R_L = 1.

452



453

454 **Fig. 2 | Fragment residence measured from orbital decay.** a, Distribution of the effective mass-to-
455 area ratio, fitted to the observed decrease of semi-major axis in annual element sets (2007–2026), for
456 fragments with radar cross-section below (blue, n = 4,855) and above (red, n = 78) 0.1 m^2 (fragments
457 whose semi-major axis decreased by at least 50 m). b, Interquartile range (bars), median (circles) and
458 mean (crosses) for each fragment cloud and size class. Dotted line: SBM mean; dashed line: value
459 assumed by Kessler and Lewis. The effective values include the effect of the atmosphere model, so that
460 they set fragment residence exactly as it enters R_L.

461

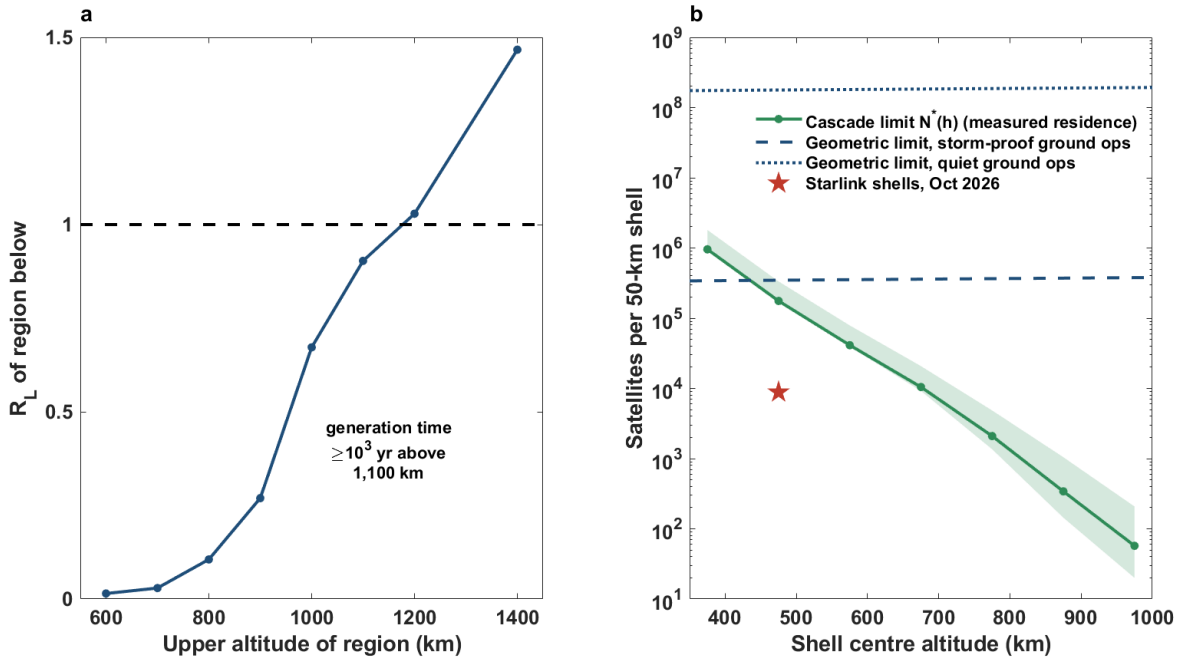


Fig. 3 | Above about 430 km, the debris cascade, not geometry, limits how many satellites a shell can host. a, R_L of the region below a given altitude. Above about 1,100 km fragment lifetimes exceed a thousand years. Values above 1,000 km rely on residence times extrapolated beyond the calibrated altitudes and are indicative only. b, Cascade limit $N^*(h)$: the number of new satellites (failure rate 1% per year, avoidance success 0.999) that a 50-km shell can host before R_L reaches unity, using the measured mean residence (line) and the median and longest-lived-cloud values (band). Dashed and dotted lines: geometric (traffic) limits from lattice shells (sun-synchronous lattice coefficient, 5.6 (a/d) ln(a/d) per shell) for storm-proof (in-shell separation 42 km, radial 0.67 km) and quiet (1.2 km, 0.08 km) ground-based operations. Star: Starlink shells at 465–485 km in October 2026.

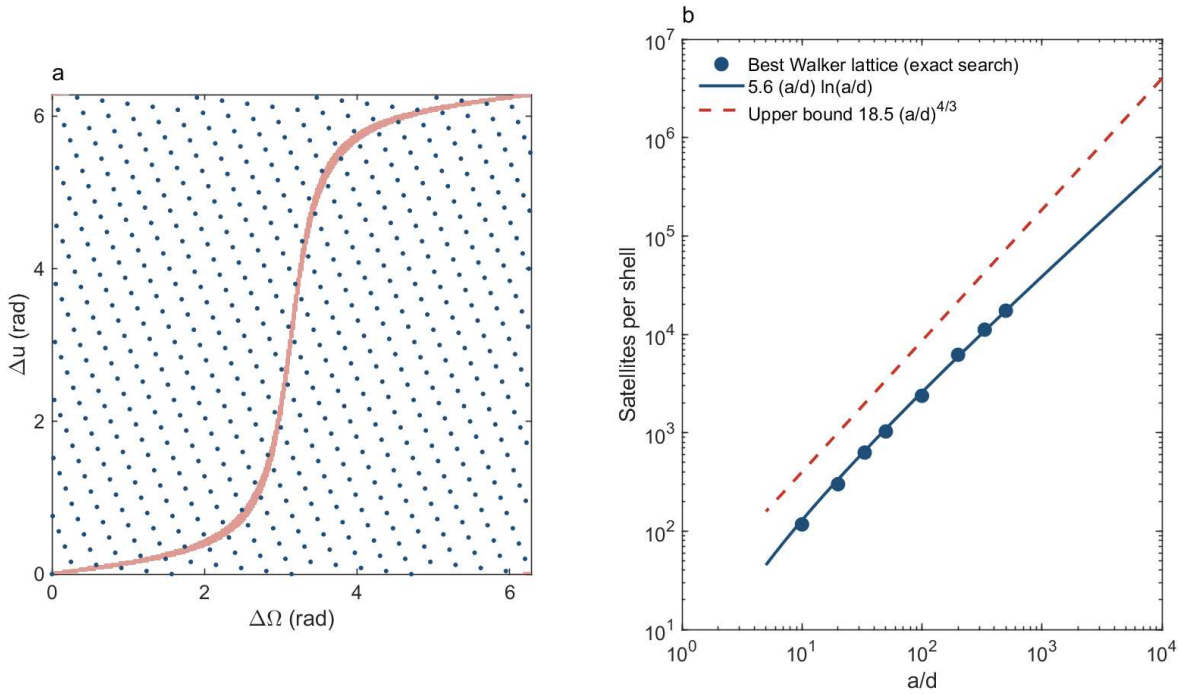
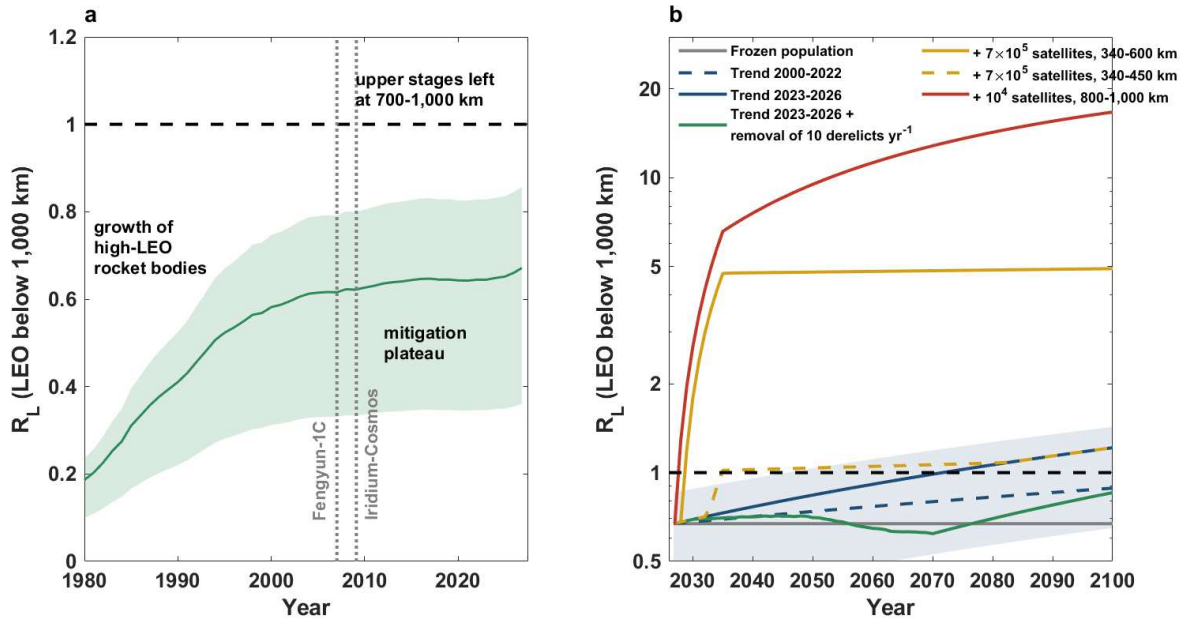


Fig. 4 | Geometric capacity of a single shell. a, Conflict band (red; $d_{min}/a < 0.03$) on the torus of node and argument-of-latitude differences for a sun-synchronous shell, and the optimal Walker lattice for this separation (628 satellites; blue). b, Satellites per shell as a function of a/d: exact optimal Walker lattices (circles, searched up to $a/d = 500$), the fit 5.6 $(a/d)\ln(a/d)$ (line) and the upper bound 18.5 $(a/d)^{4/3}$ (dashed; rigorous to leading order in d/a) for $i = 97.6°$. The achievable lattices and the bound bracket the capacity of any arrangement in the shell (the geometric scaling law).



480

481 **Fig. 5 | Past and projected reproduction number.** a, R_L of LEO below 1,000 km reconstructed from
482 launch and decay records of the catalogue (line: measured mean residence; band: median-based to
483 longest-lived cloud). Dotted lines mark the Fengyun-1C and Iridium–Cosmos breakups. b, Scenario
484 projections (mean residence): frozen 2026 population; population trends of 2000–2022 and 2023–2026
485 (band: median-based to longest-lived cloud for the latter); the 2023–2026 trend with removal of the ten
486 most massive derelicts per year from 700–1,000 km from 2030 (400 objects in total, exhausted by 2070);
487 and the 2023–2026 trend with 7×10^5 satellites at 340–600 km or 340–450 km, or 10^4 satellites at 800–
488 1,000 km, deployed over 2027–2035 with a failure rate of 1% per year. The dashed line marks $R_L = 1$.

Supplementary Files

This is a list of supplementary files associated with this preprint. Click to download.

- 2SupplementaryInformationsubmission.docx